Title
Developing Positron Range Correction for Pair Production Tomography

ISBN
9798190914924

Author
Thoreson, Isha

Publication Date
2026-09-09

Peer reviewed|Thesis/dissertation

Developing Positron Range Correction for Pair Production Tomography

by
Isha Thoreson

THESIS
Submitted in partial satisfaction of the requirements for degree of
MASTER OF SCIENCE

in

Biomedical Imaging

in the

GRADUATE DIVISION
of the
UNIVERSITY OF CALIFORNIA, SAN FRANCISCO

Approved:

Signed by:
Qihui Lyu
8999354EC122454...
Chair

Signed by:
Ke Sheng

Jose Ramos Mendez

Jessica Scholey
67DFAA085656407...

Committee Members

Developing Positron Range Correction for Pair Production Tomography

Isha Thoreson

ABSTRACT

Pair Production Tomography (P2T) is an emerging imaging modality that detects pair production events from high-energy photon beams, providing unique atomic-number-based contrast. A fundamental challenge in P2T image reconstruction is positron range — the finite distance positrons travel before annihilating — which causes spatial blurring between the true pair production distribution and the reconstructed annihilation image. Unlike PET, the directed photon beam in P2T breaks the isotropy of positron emission, requiring a beam-direction-dependent correction approach. No positron range correction method has previously been developed for P2T.

In this work, two positron range correction methods are developed and evaluated for P2T imaging: Richardson-Lucy deconvolution and a TV-regularized optimization framework solved using the Fast Iterative Shrinkage-Thresholding Algorithm (FISTA). Beamlet-specific positron range kernels were constructed from Geant4 Monte Carlo simulations using a 10MV bremsstrahlung source, capturing the joint distribution of transverse positron displacement and emission angle relative to the beam direction. Kernels were constructed at three resolutions — 2mm, 1mm, and 0.5mm — to evaluate the effect of kernel resolution on correction performance.

Corrections were applied to all 46 beamlets of a simulated CT-based phantom containing three high-Z inserts. Both methods consistently improved beam profile spatial accuracy across all 46 beamlets, reducing average beam full width at half maximum (FWHM) from 8.5mm to

approximately 6mm. At the full image level, pseudo-high resolution reconstruction at 1mm followed by rebinning to the intrinsic 2mm detector resolution was found to be the optimal pipeline. Both Richardson-Lucy and FISTA reduced insert FWHM from 18mm to 16mm with the 1mm resolution kernel correction. Direct 2mm reconstruction and correction showed no improvement in insert FWHM, demonstrating the importance of kernel resolution for accurate correction.

These results demonstrate that positron range correction is feasible for P2T imaging and can meaningfully improve spatial resolution. The current pipeline represents a practical and effective approach, providing a foundation for future development of spatially varying kernels and expansion to full-view phantom and patient data.

TABLE OF CONTENTS

LIST OF FIGURES

LIST OF TABLES

INTRODUCTION

Pair production tomography (P2T) is an imaging modality that uses the pair production interaction of high-energy photon beams with tissue. When photons with energies exceeding 1.022 MeV interact with matter, they can undergo pair production, generating a positron-electron pair. The positron subsequently annihilates with a nearby electron, producing two 511 keV gamma photons emitted in opposite directions. These coincident photons are detected by a ring detector, similar to positron emission tomography (PET), enabling tomographic reconstruction of the pair production distribution along the beam path.

Unlike conventional X-ray computed tomography (CT), which forms images based on photon attenuation and is primarily sensitive to tissue density, P2T provides unique atomic number-based contrast, allowing detection of high-Z contrast agents or materials. The feasibility of P2T imaging was first demonstrated using Monte Carlo simulations of tissue-mimicking phantoms [1].

A fundamental challenge in P2T image reconstruction is positron range, the finite distance positrons travel before annihilating. Since the ring detector localized the annihilation site rather than the pair production site, the reconstructed image is spatially blurred relative to the true pair production distribution. This blurring limits the spatial resolution and accuracy of P2T images.

Like CT, P2T images material composition along the beam path. However, P2T provides capabilities distinct from conventional CT with material contrast that is linear to atomic number [1]. This linearity enables differentiation of materials that appear similar in CT, and P2T images can be formed even with partial-view and sparse-view projections. For this imaging application, spatial accuracy of the reconstructed image is important – positron range blurring reduces the ability to accurately localize pair production events and distinguish material boundaries. Positron range correction aims to recover this spatial accuracy by bringing the reconstructed annihilation image closer to the true pair production distribution.

Positron range correction has been studied in the PET literature to recover spatial resolution lost due to positron range blurring. Methods include incorporating the positron range distribution into the iterative reconstruction process and post-reconstruction process [2, 3]. A key difference between P2T and PET is that the directed photon beam breaks the isotropy of positron emission. In PET, positrons are emitted isotropically, allowing radially symmetric kernels. In P2T, the positron range distribution depends on the angle relative to the beam direction, requiring a beam-direction-dependent joint distribution. Figure 1 displays the distribution of positron annihilation positions relative to the pair production site, demonstrating the anisotropic nature of positron travel in P2T. No positron range correction method has been developed for P2T.

In this work, we develop and evaluate two positron range correction methods, Richardson-Lucy deconvolution and an optimization framework solved using the Fast Iterative Shrinkage-Thresholding Algorithm (FISTA), for P2T images.

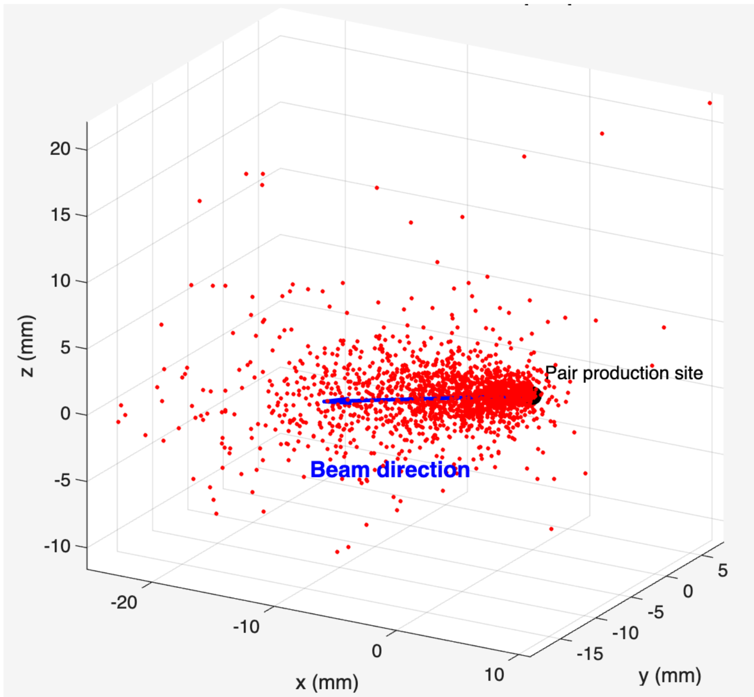

Figure 1: Simulated three-dimensional positron annihilation distribution relative to the pair production site (black dot) for a 10MV bremsstrahlung beam (blue arrow). The elongated distribution along the beam direction demonstrated the anisotropic nature of positron range in P2T.

METHODS

Simulation and Data

All data used in this work was obtained from Monte Carlo simulation – no experimental measurements were performed. All simulations were performed using Geant4 [4], a Monte Carlo particle transport toolkit. Two separate simulations were conducted: a full reconstruction simulation and a standalone beamlet simulation.

The full reconstruction simulation used two photon beams at gantry angles of 114° and 294°, comprising 46 beamlets total (22 in beam 1, 24 in beam 2). Each beamlet was simulated with using a 10MV bremsstrahlung x-ray energy spectrum. The simulation geometry was based on a CT phantom containing three high-Z inserts. For each simulated pair production event, the positron position was recorded, giving the location of pair production in 3D space. Detected coincidence events were recorded for image reconstruction.

The standalone kernel simulation used a single beamlet with the same 10MV bremsstrahlung source. In addition to the positron positions, the positron trajectory data were recorded, including the total positron range r, momentum direction (px, py, pz), and annihilation position. This data was used to characterize the positron range distribution and construct the correction kernel.

Kernel Construction

To correct for positron range effects in P2T images, a beamlet-specific positron range kernel must be constructed. The kernel characterizes the probability distribution of positron annihilation locations relative to the pair production site. Because the directed photon beam breaks the isotropy of positron emission, the 2D kernel is constructed as a function of two variables: the transverse positron displacement, $r_{\perp}$, and the emission angle, θ, relative to the beam direction. The joint distribution $\mathrm{F}(r_{\perp}, \theta)$ is estimated from the standalone simulation positron trajectory data.

For each simulated positron, the transverse displacement, $r_{\perp}$, is computed as the component of the total range perpendicular to the beam direction, and the emission angle θ is computed as the angle between the positron momentum direction and the beam direction. The mathematical expressions used to determine $r_{\perp}$ and θ are

$$r_{\perp} = \sqrt{r^2 - (r \cdot \hat{b})^2} \tag{1}$$

$$\theta = \cos^{-1}\left(\frac{(p_x, p_y, p_z)}{|(p_x, p_y, p_z)|} \cdot \hat{b}\right) \tag{2}$$

where r is the total positron range, (p_x, p_y, p_z) is the positron momentum direction, and $\hat{b}$ is the unit vector along the beam direction. The joint histogram $\mathrm{F}(r_{\perp}, \theta)$ is estimated from all simulated positron trajectories after removing duplicate events.

A separate kernel is constructed for each of the 46 beamlets using the same $\mathrm{F}(r_{\perp}, \theta)$ distribution. Rather than re-running the simulation for each beamlet, the shared $\mathrm{F}(r_{\perp}, \theta)$ histogram is reused and sampled onto a 2D pixel grid oriented along each beamlet's specific direction. For each pixel at position (x,y) relative to the pair production site, the corresponding polar coordinates $(r_{\perp}, \theta)$ are computed based on the beamlet direction, and the kernel value k(x,y) is obtained by bilinear interpolation from $\mathrm{F}(r_{\perp}, \theta)$,

$$k(x, y) = F(r_{\perp}(x, y), \theta(x, y)). \tag{3}$$

The kernel is then normalized so that all values sum to one,

$$\sum k(x, y) = 1. \tag{4}$$

This approach assumes that the positron range distribution is the same for all beamlets – an approximation that holds when tissue composition is approximately uniform across the beam paths. Kernels were constructed at three resolutions: 2mm, 1mm, and 0.5mm, using the same F($r_\perp$, θ) distribution.

Positron Range Correction

Positron range correction is applied independently to each beamlet reconstruction using the beamlet-specific kernel. Two correction methods are implemented and evaluated.

The first method is Richardson-Lucy deconvolution with Total Variation (TV) regularization [5,6,7]. Richardson-Lucy is an iterative algorithm that updates the current image estimate according to

$$f^{t+1} = \frac{f^t}{1-\lambda \cdot TV(f^t)} \cdot \left(k^T \otimes \frac{g}{k \otimes f^t}\right) \tag{5}$$

where f^t is the current estimate of the true image at iteration t, g is the observed blurry image, k is the beamlet-specific positron range kernel, k^T denotes the flipped kernel, and λ controls the strength of the TV regularization.

The second method frames the correction as a regularized optimization problem. For each beamlet, the corrected image f is obtained by minimizing

$$\frac{1}{2} \|k \otimes f - g\|^2 + \lambda \cdot TV(f), \quad \textit{subject to } f \geq 0 \tag{6}$$

This optimization problem is solved using the Fast Iterative Shrinkage-Thresholding Algorithm (FISTA) [8]. Both methods are run for 20 iterations with regularization parameter $\lambda = 0.01$ on each beamlet image with the beamlet-specific kernel.

Image Reconstruction

Time-of-flight (TOF) direct reconstruction is performed independently for each of the 46 beamlets using detected coincidence events from the Geant4 simulation. Attenuation correction is incorporated into the reconstruction using the CT-based phantom geometry. Positron range correction is then applied to each beamlet reconstruction using the beamlet-specific kernel. The corrected beamlet images are summed to produce the full pair production image.

The intrinsic detector resolution is 2mm, and the baseline reconstruction was performed at this resolution to investigate whether a more accurate kernel representation improved correction performance, reconstructions were also performed at higher resolutions of 1mm and 0.5mm, with corresponding kernels constructed at each resolution. Reconstruction at finer pixel sizes allows the kernel to better capture sub-pixel variations in the positron range distribution, potentially, enabling more accurate correction. For the 1mm and 0.5mm reconstructions, the final corrected image is rebinned to 2mm to match the intrinsic resolution.

Imaging Setup

The imaging phantom used in this work is a CT-based cylindrical phantom containing three high-Z inserts: iodine, ytterbium, and bismuth. These high-Z materials produce strong pair production contrast relative to the surrounding phantom material, making them useful targets for evaluating the spatial accuracy of the correction.

Two photon beams were simulated, comprising 46 beamlets total. Gantry angles of 114° and 294° were chosen arbitrarily, with the two beams separated by 180° to image the same portion of the phantom cross-section from opposing directions. Together the two beams provide partial coverage of the phantom cross-section, with each beamlet subtending a small angular range. Coincidence detection was performed using a simulated ring detector with an inner radius of 120cm and axial height of 10cm, comprising 1440 detector crystals. The simulation assumed 100% detector efficiency. Reconstruction is performed on a single axial slice through the phantom center.

The ground truth pair production distribution was generated by binning the positron pair production positions from the full reconstruction simulation into the same 2D pixel grid used for image reconstruction. This gives the true spatial distribution of pair production events, which serves as the reference for evaluating correction performance.

RESULTS

Kernel Characterization

The positron range and emission angle distributions obtained from the standalone Geant4 simulation are shown in Figures 2 and 3. Positrons have a median range of 2.7mm, with a tail extending to longer ranges. The emission angle distribution peaks at approximately 19° from the beam direction, confirming the anisotropic nature of positron emission in P2T.

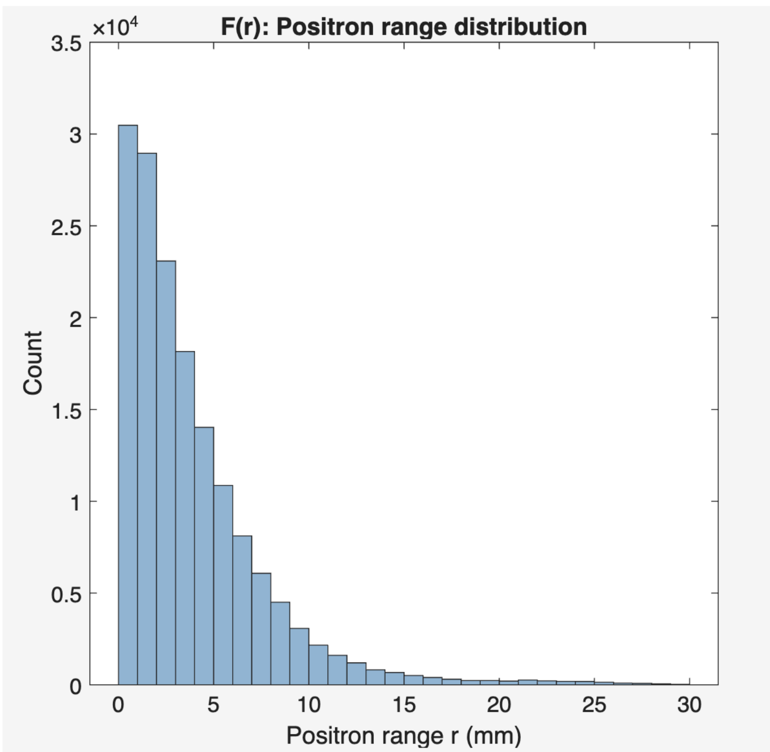

Figure 2: Positron range distribution from the single beamlet Geant4 simulation. The median positron range is 2.7mm.

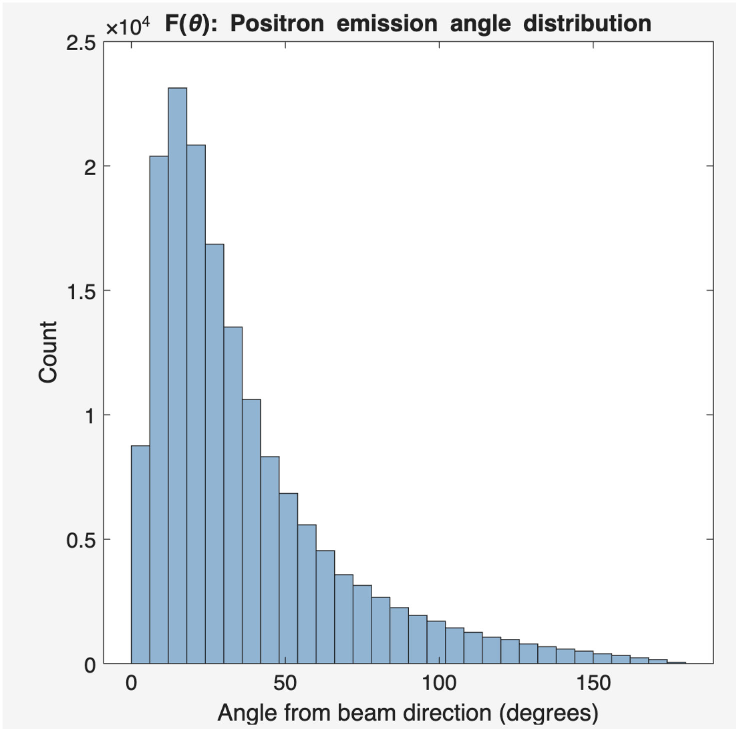

Figure 3: Emission angle distribution of positrons relative to the beam direction from single beamlet Geant4 simulation. The distribution peaks at approximately 19°**.**

The anisotropy is further captured in Figure 4, the joint distribution F($r_{\perp}$, θ), which shows a clear concentration of events at small transverse displacements and emission angles near 19°. The 2D kernel in Figure 5 is elongated and asymmetric – unlike the radially symmetric kernels used in PET – reflecting the preferential forward emission of positrons along the beam direction.

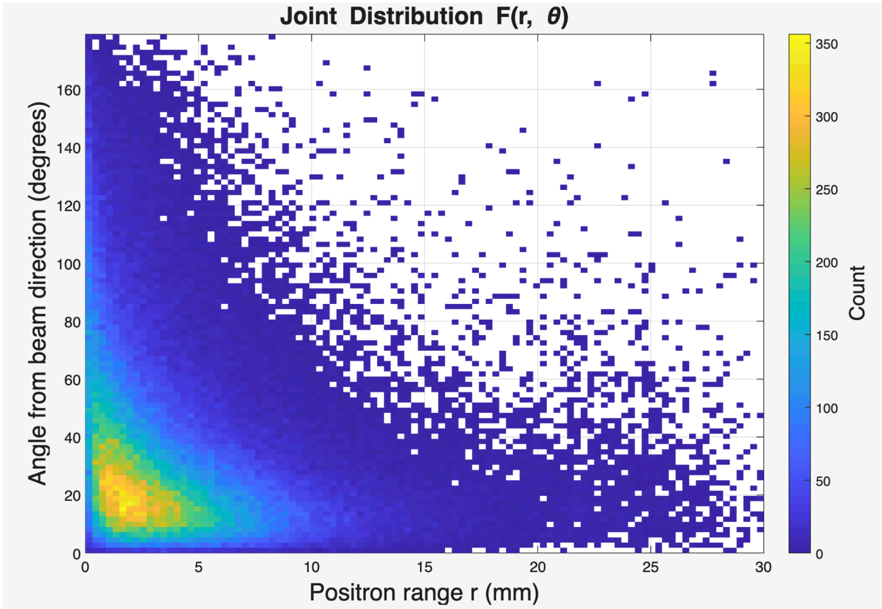

Figure 4: Joint distribution, F($r_{\perp}$, θ), of transverse positron displacement and emission angle relative to the beam direction, estimated from the standalone Geant4 simulation.

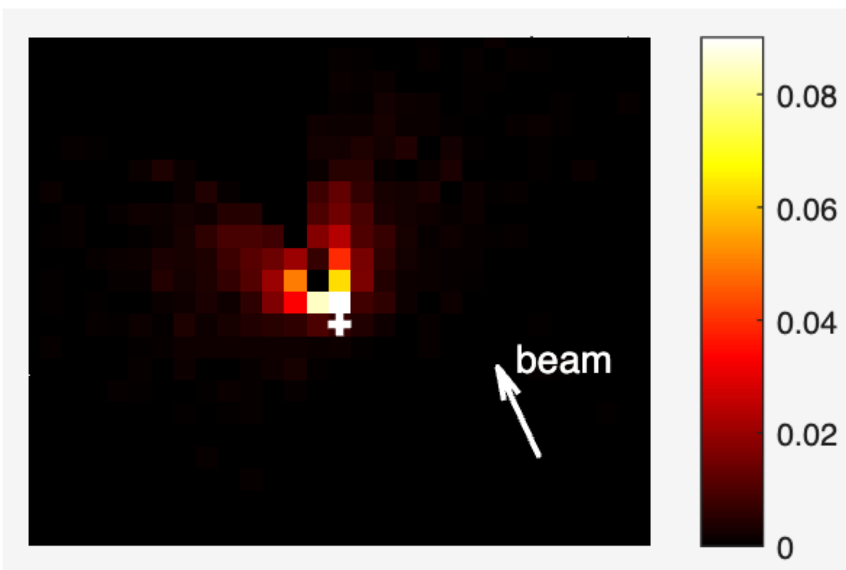

Figure 5: 2D positron range kernel for beam 1, beamlet 6 at 1mm resolution, oriented along the beamlet direction.

Single Beamlet Results

Positron range correction was applied to all 46 beamlet reconstructions using both Richardson-Lucy and FISTA solved optimization methods. Figure 6 shows the ground truth pair production distribution, uncorrected image, and corrected images for a representative beamlet (beam 1, beamlet 11). Both corrected images show a visually narrower beam profile compared to the uncorrected image, moving toward the ground truth distribution.

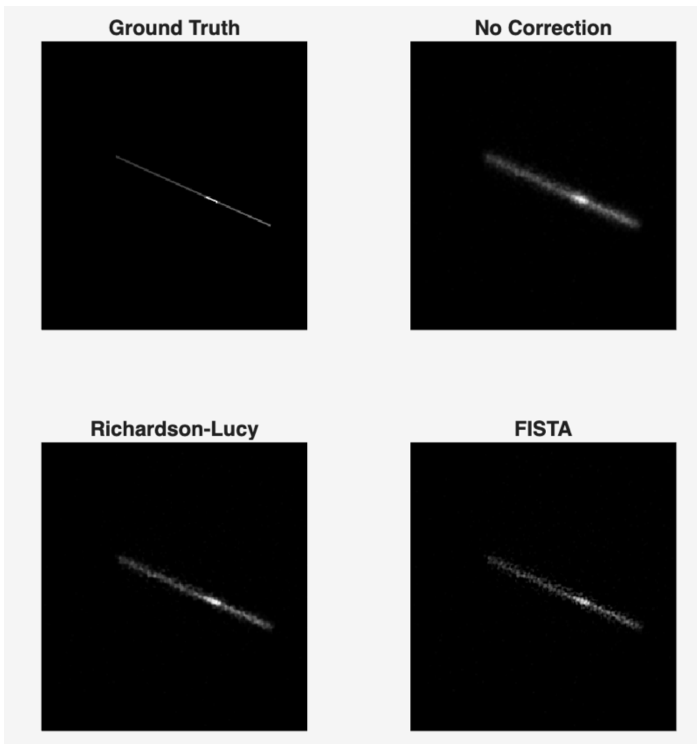

Figure 6: Ground truth pair production distribution, uncorrected image, Richardson-Lucy corrected image, and FISTA corrected image for a single beamlet. Both correction methods show a visually narrower beam profile compared to the uncorrected image.

To quantify the spatial improvement, a line profile through the beamlet at column 178 is shown in Figure 7. The uncorrected beam has a FWHM of 7mm at this location, while Richardson-Lucy and FISTA reduce this to 5mm and 3mm, compared to a ground truth FWHM of 2mm.

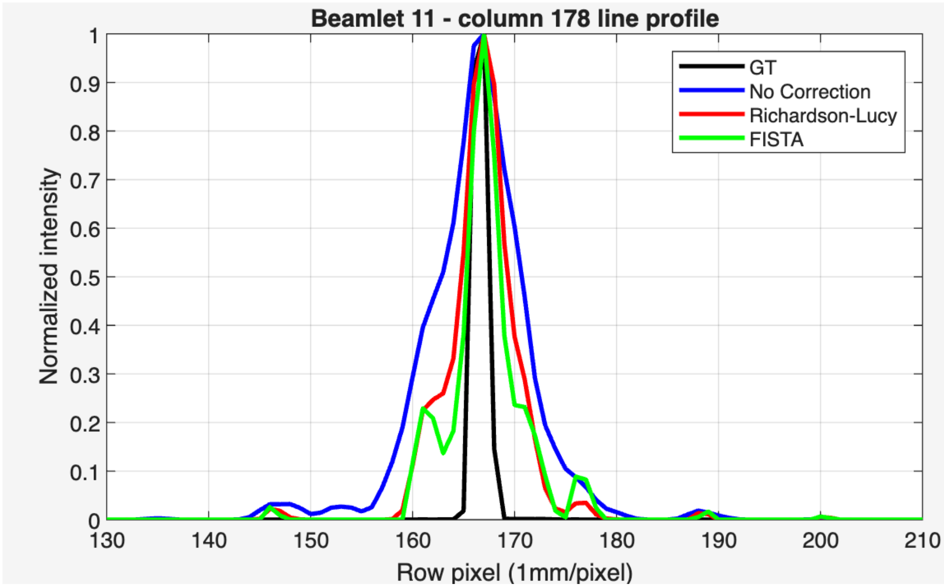

Figure 7: Line profile through a single beamlet. The corrected images show narrower beam profiles compared to the uncorrected image, moving toward the ground truth (black).

To evaluate consistency across all beamlets, beam profile FWHM was computed at column 178 for all 46 beamlets. The average beam FWHM reduced from 8.5mm without correction to 6.1mm with Richardson-Lucy and 6.0mm with FISTA (Table 1). Both methods improved the beam FWHM for all 46 beamlets with no beamlet having a wider profile after correction.

Table 1: Beam profile FWHM for a single beamlet and averaged across all 46 beamlets. FWHM measured at the midpoint between peak and background intensity.

Method	**Single beamlet profile FWHM**	**Average across all beamlets**
Ground Truth	2mm	2mm
No Correction	7mm	8.5mm
Richarson-Lucy	5mm	6.1mm
FISTA	3mm	6.0mm

Full Image Results

The full pair production image is produced by summing all 46 corrected beamlet reconstructions. Figure 8 shows the ground truth pair production distribution, uncorrected image, and corrected images for the full reconstruction, with corrections applied at 1mm resolution and rebinned to the 2mm image resolution. Both corrected images show improved sharpness compared to the uncorrected image, with more clearly defined phantom boundaries and insert regions.

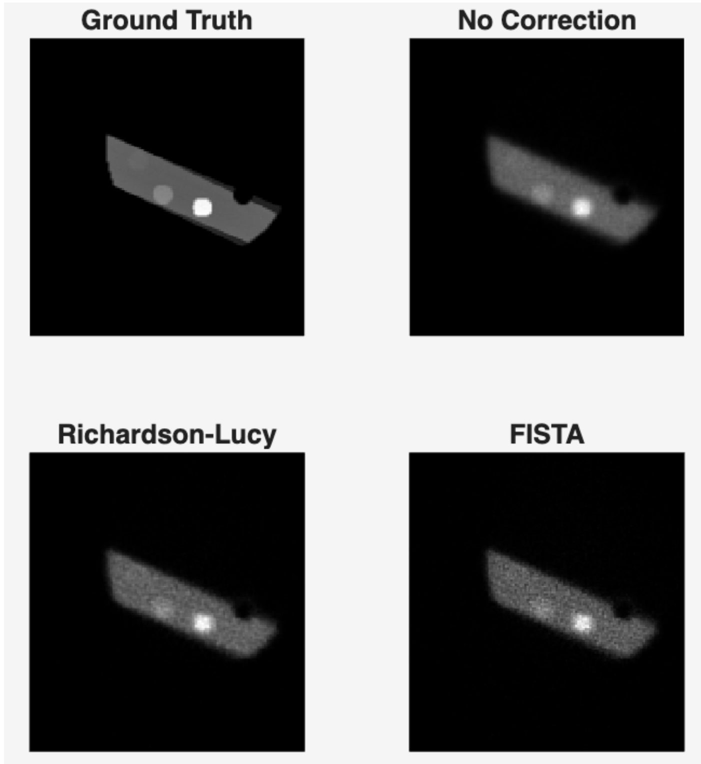

Figure 8: Ground truth pair production distribution, uncorrected image, Richardson-Lucy corrected image, and FISTA corrected image for the full pair production reconstruction.

A line profile through the insert region at row 91 is shown in Figure 9. The corrected images show a narrower insert peak compared to the uncorrected image, moving toward the ground truth profile. The insert FWHM, measured at the midpoint between peak and background intensity, is shown in Table 2. Without correction the insert appears 18mm wide, while both Richardson-Lucy and FISTA reduce this to 16mm compared to a ground truth of 14mm. The phantom edge width, measured at the 5% intensity threshold, also improved with correction. Without correction the phantom boundary extends to 120mm, while Richardson-Lucy and FISTA reduce this to 114mm compared to a ground truth of 108mm.

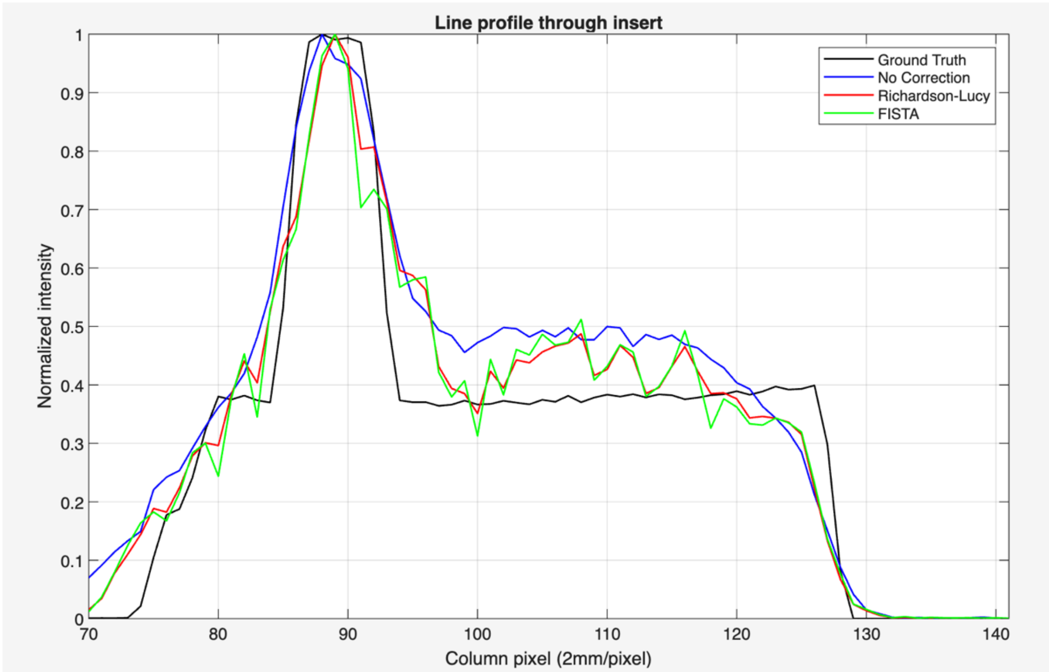

Figure 9: Line profile through the insert region at row 91 of the full pair production image. Corrected images show narrower insert peaks compared to the uncorrected image, moving toward the ground truth profile (black).

Table 2: Insert FWHM and phantom edge width for the full image reconstruction. FWHM measured at midpoint between peak and background intensity. Phantom edge width measured at 5% intensity threshold.

Method	Insert FWHM	Phantom Width
Ground Truth	14mm	108mm
No Correction	18mm	120mm
Richarson-Lucy	16mm	114mm
FISTA	16mm	114mm

Resolution Comparison

To evaluate the effect of kernel resolution on correction performance, the full image pipeline was run at three resolutions: 2mm reconstruction at the detector resolution, 1mm resolution corrected and rebinned to 2mm, and 0.5mm resolution corrected and rebinned to 2mm. Figure 10 shows the full pair production images for all three reconstructions, and Figure 11 shows the corresponding line profiles through the insert region.

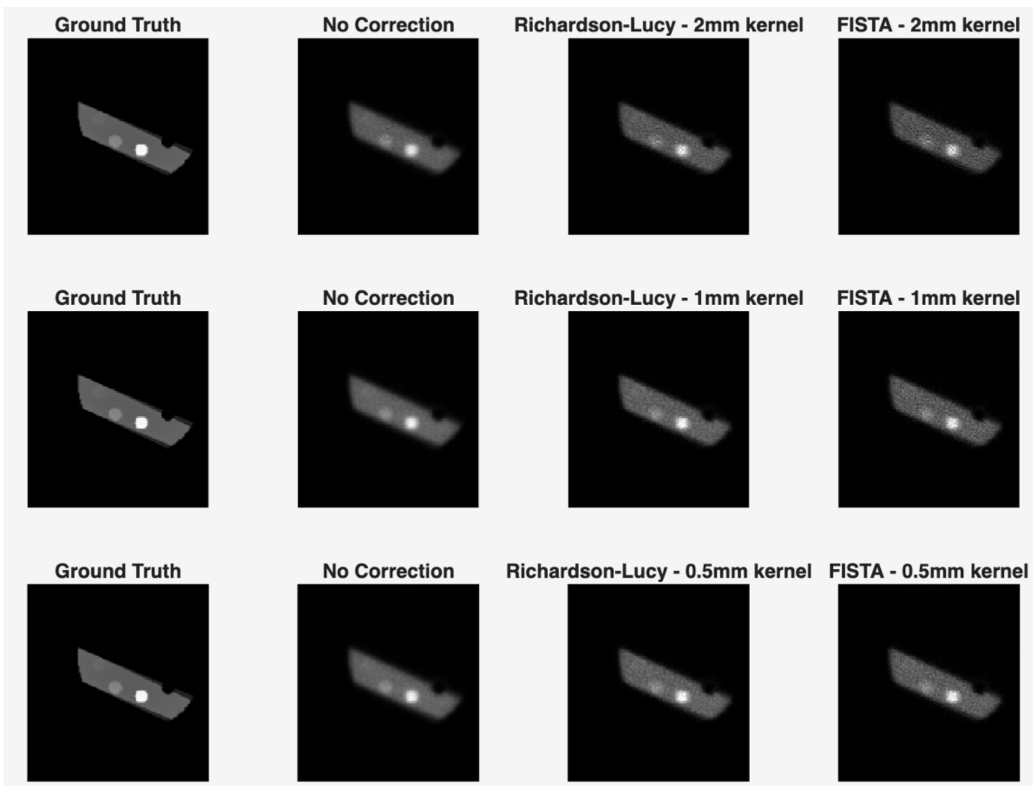

Figure 10: Full pair production images for all three kernel resolution corrections – 2mm resolution, 1mm resolution correction, and 0.5mm resolution correction. Ground truth, uncorrected, Richardson-Lucy correct, and FISTA corrected images are shown for each resolution.

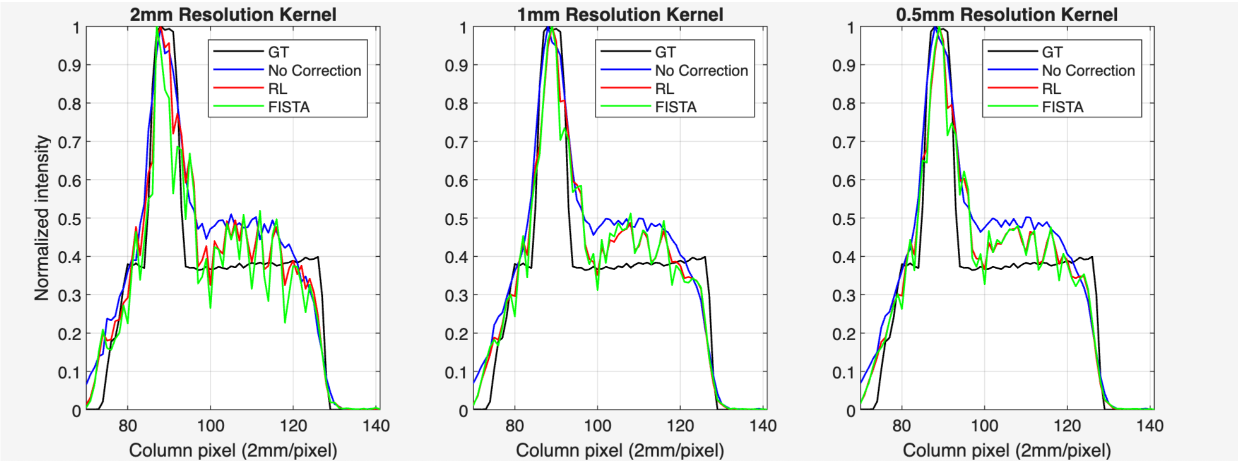

Figure 11: Line profiles through the insert region at row 91 for all three kernel resolution corrections. The 1mm and 0.5mm results show narrower insert peaks compared to direct 2mm reconstruction.

The insert FWHM and phantom edge width results for all three reconstructions are summarized in Table 3. Direct 2mm reconstruction and correction showed no improvement in insert FWHM for either method, remaining at 18mm compared to the ground truth of 14mm. Correcting at 1mm and rebinning to 2mm reduced the insert FWHM to 16mm for both Richardson-Lucy and FISTA. Correcting at 0.5mm and rebinning to 2mm further reduced the FISTA insert FWHM to 14mm, matching the ground truth, while Richardson-Lucy remained at 16mm. Signal-to-noise ratio was also computed for all three pipelines. The higher resolution corrected reconstructions show higher SNR than direct 2mm reconstruction for all methods, suggesting that 2mm resolution kernel is too coarse to preserve the positron range variation and can lead to increased noise in the images.

Table 3: Insert FWHM and SNR for all three kernel resolution reconstructions. FWHM measured at midpoint between peak and background intensity.

Method	**2mm Kernel**		**1mm Kernel**		**0.5mm Kernel**	
	FWHM	SNR	FWHM	SNR	FWHM	SNR
Ground Truth	14mm	--	14mm	--	14mm	--
No Correction	18mm	197.0	18mm	197.0	18mm	197.0
Richarson-Lucy	18mm	178.9	16mm	196.7	16mm	195.3
FISTA	18mm	112.4	16mm	127.6	14mm	134.0

DISCUSSION

Interpretation of Per-beamlet vs Full Image Results

Positron range blurs the reconstructed image from the true pair production locations, causing phantom structures, such as the high-Z inserts, to appear wider than their true size. Positron range correction is expected to reverse this effect, reducing the apparent insert width toward the ground truth. Positron range correction consistently improved beam profile FWHM, reducing average beam FWHM from 8.5mm to approximately 6mm, confirming the correction is working as expected.

At the full image level, both methods reduced insert FWHM when corrections were applied at 1mm or 0.5mm resolution. However, direct 2mm correction showed no improvement in insert FWHM, suggesting that the 2mm kernel lacks the resolution to accurately capture positron range variations, especially within the first 2mm of the range distribution where there is significant variation. The 2mm resolution correction also showed lower SNR compared to the higher resolution corrections. The coarser 2mm kernel cannot resolve fine variations in the positron range distribution, resulting in events being corrected by less precise displacement amounts – grouped into coarser 2mm increments rather than the more accurate displacements captured by the higher resolution kernels. This less precise correction leads to increased image noise and spottiness in the image.

As shown in Figure 11, the line profiles for corrected images from 2mm and 1mm reconstructions appear visually different, while the line profiles for the 1mm and 0.5mm reconstructions are nearly identical, suggesting that the improvement in kernel accuracy from 2mm to 1mm is more significant than from 1mm to 0.5mm. Higher resolution kernels provided better correction accuracy, however, since 1mm and 0.5mm produce similar results, and the 0.5mm reconstruction required approximately 2.5x more computational time due to the larger image size, 1mm represents the best balance between correction accuracy and computational cost. This computational cost will increase further when the method is extended to full phantom coverage or patient data with more beamlets and larger fields of view.

Clinical Feasibility

A rough dose estimation was performed to assess the imaging dose required under more realistic detector conditions. The simulation used 100% detector efficiency – to achieve equivalent image quality with a more realistic efficiency of 10%, an estimated imaging dose of approximately 0.02 cGy total for all 46 beamlets would be required. This dose estimate would increase in situations with larger field of view requiring more beamlets, but nevertheless suggests that P2T imaging can achieve this image quality at a dose level that would be safe for patients.

Limitations

The current kernel assumes uniform positron travel across the entire beamlet, which does not account for spatially varying material density. In reality, positrons stop faster in denser high-Z materials such as the phantom inserts compared to surrounding tissue. This uniform travel approximation limits correction accuracy in regions where material density differs significantly from the average density assumed by the kernel.

Apart from imaging atomic number, P2T has relevant applications in real-time radiation dose monitoring during radiotherapy. For dose monitoring applications, the clinical significance of positron range correction is less clear. Whether correction meaningfully improves dose verification accuracy would require further investigation. Additionally, the computational time required for correction may present challenges for real-time applications.

All results were obtained from a controlled Monte Carlo simulation environment. Extension to real patient data would introduce additional challenges that are not present in this simulation, including beam hardening effects at greater tissue depths which would alter the photon energy spectrum and therefore the positron range distribution at different depths, and larger field of view with more beamlets increasing computational intensity of a per-beamlet reconstruction. These factors would need to be addressed in the future stages of this project.

Future Directions

Future work will focus on implementing a spatially varying kernel to account for material-dependent positron behavior, which would better handle variations positron behavior in different materials. Expanding the method to a full-view phantom with more beamlets and larger field of view would be an important next step towards application on patient data.

CONCLUSION

This work developed and evaluated two positron range correction methods – Richardson-Lucy deconvolution and a TV-regularized optimization framework solved using FISTA – for Pair Production Tomography imaging. Beamlet-specific positron range kernels were constructed from Geant4 Monte Carlo simulations using a 10MV bremsstrahlung source, capturing the anisotropic positron range distribution characteristic of P2T. Positron range correction improved image spatial accuracy, as evaluated through phantom insert width measurements. Higher resolution correction at 1mm was found to provide a more accurate kernel correction, with both methods showing improved insert width recovery compared to direct 2mm reconstruction and correction. These results demonstrate that positron range correction is feasible for P2T imaging and can meaningfully improve image accuracy, although the directed nature of the photon beam requires correction methods distinct from those used in PET. This work represents a foundation for future development of positron range correction methods for P2T.

REFERENCES

[1] Lyu, Q., Neph, R., & Sheng, K. (2023). Tomographic detection of photon pairs produced from high-energy X-rays for the monitoring of radiotherapy dosing. *Nature Biomedical Engineering*, 7, 323–334.

[2] Bai, B., Ruangma, A., Laforest, R., Tai, Y. C., & Leahy, R. M. (2003). Positron range modeling for statistical PET image reconstruction. *IEEE Nuclear Science Symposium Conference Record*, 4, 2501–2505.

[3] Bertolli, O., Eleftheriou, A., Cecchetti, M., Tsoumpas, C., & Visvikis, D. (2016). PET iterative reconstruction incorporating an efficient positron range correction method. *Physica Medica*, 32, 323–330.

[4] Agostinelli, S., et al. (2003). Geant4 — a simulation toolkit. *Nuclear Instruments and Methods in Physics Research A*, 506(3), 250-303.

[5] Lucy, L. B. (1974). An iterative technique for the rectification of observed distributions. *The Astronomical Journal*, 79, 745–754.

[6] Richardson, W. H. (1972). Bayesian-based iterative method of image restoration. *Journal of the Optical Society of America*, 62(1), 55–59.

[7] Dey, N., Blanc-Feraud, L., Zimmer, C., Roux, P., Kam, Z., Olivo-Marin, J. C., & Zerubia, J. (2006). Richardson-Lucy algorithm with total variation regularization for 3D confocal microscope deconvolution. *Microscopy Research and Technique*, 69(4), 260–266.

[8] Beck, A., & Teboulle, M. (2009). A fast iterative shrinkage-thresholding algorithm for linear inverse problems. *SIAM Journal on Imaging Sciences*, 2(1), 183–202.

Publishing Agreement

It is the policy of the University to encourage open access and broad distribution of all theses, dissertations, and manuscripts. The Graduate Division will facilitate the distribution of UCSF theses, dissertations, and manuscripts to the UCSF Library for open access and distribution. UCSF will make such theses, dissertations, and manuscripts accessible to the public and will take reasonable steps to preserve these works in perpetuity.

I hereby grant the non-exclusive, perpetual right to The Regents of the University of California to reproduce, publicly display, distribute, preserve, and publish copies of my thesis, dissertation, or manuscript in any form or media, now existing or later derived, including access online for teaching, research, and public service purposes.

Signed by:
Isha Thoreson
C14C16F64A034FF...
Author Signature

09/01/2026
Date